

Mesophase Ordering of TiO₂ Film with High Surface Area and Strong Light Harvesting for Dye-Sensitized Solar Cell

S. Agarwala,[†] M. Kevin,[†] A. S. W. Wong,[‡] C. K. N. Peh,[†] V. Thavasi,[§] and G. W. Ho^{*,†}

Department of Electrical and Computer Engineering, National University of Singapore, Singapore 117576, Institute of Materials Research and Engineering, ASTAR (Agency for Science Technology and Research), 3 Research Link, Singapore 117602, and Nanoscience and Nanotechnology Initiative, Faculty of Engineering, National University of Singapore, Engineering Drive 3, University Hall, Singapore 117576

ABSTRACT Mesophase ordering and structuring are carried out to attain optimized pore morphology, high crystallinity, stable porous framework, and crack-free mesoporous titanium dioxide (TiO₂) films. The pore structure (quasi-hexagonal and lamellar) can be controlled via the concentration of copolymer, resulting in two different types of micellar packing. The calcination temperature is also controlled to ensure a well-crystalline and stable porous framework. Finally, the synthesized mesoporous TiO₂ film is modified by adding P25 nanoparticles, which act as scattering centers and function as active binders to prevent formation of microcracks. Adding P25 nanoparticles into mesoporous structure helps to provide strong light-harvesting capability and large surface area for high efficiency dye-sensitized solar cells (DSSC). The short-circuit photocurrent density (j_{sc}) of the cell made from mixture of mesoporous TiO₂ and P25 nanoparticles displays a higher efficiency of ~6.5% compared to the other homogeneous films. A combination of factors such as increased surface area, introduction of light-scattering particles, and high crystallinity of the mesoporous films leads to enhanced cell performance.

KEYWORDS: mesoporous • titanium dioxide • dye-sensitized solar cells • light-scattering • self-assembly

1. INTRODUCTION

DSSCs based on the nanocrystalline TiO₂ have been widely researched because of their low production cost and high conversion efficiencies (1–4). Among the many morphologies adopted for DSSC (5–8), ordered mesoporous metal oxides have received extensive attention because of their high surface area and uniform pore structure. Mesoporous TiO₂ is of particular interest here for its widespread use in chemical and gas sensing, electrochromic devices, optical waveguides, optical catalysts, and photovoltaics (1, 9–15).

Sol–gel process using the template assembly of organic surfactants is the most common route taken for synthesis of mesoporous TiO₂. This process is highly manufacturable because it is low temperature, highly scalable, and does not require any expensive or extensive equipment. Here, inorganic titanium precursors are dispersed in cationic or non-ionic systems and then spin-coated on the substrate, followed by calcination of the film. Pioneer work has been

carried out by Stucky (16, 17), Wiesner (18, 19), and Coakley (20) in controlling the morphology of materials by using block copolymers. Recently, Kaune et al. (21) also reported on the preparation of hierarchically structured TiO₂ films by colloidal templating. These works have been successfully incorporated in making efficient DSSC (22–24). P123 templated mesoporous TiO₂ is shown to give an efficiency of 4.04% (22). When nonionic surfactant Tween 20 is used, the energy conversion efficiency can be enhanced to 6% (23). Wiesner et al. studied the role of different TiO₂ morphologies using polyisoprene-block-ethyleneoxide (PI-b-PEO) copolymer and demonstrated its use in DSSC (24).

A few more issues must be addressed to efficiently apply the ordered TiO₂ films for solar cells. First, the films must have an optimum thickness for better light absorption (25). Second, the films must be crystalline for efficient transfer of the injected electrons (2). Third, the films should have high surface area for better dye adsorption (26). It is well-known that the solution-based synthesis of mesoporous TiO₂ can normally achieve a few hundreds of micrometers thickness. Repeated spin- and dip-coating with subsequent calcination is employed to obtain thick TiO₂ films (24, 27–29). Apart from being time-consuming, the repetitive coating and sintering procedures lead to degradation of the film's mesostructure, eventually leading to cracks in the film (30). Although, recently Wiesner et al. has successfully demonstrated synthesis of porous TiO₂ at high temperature by soft and hard (CASH) method (31). It is also important to note that the high surface area can be achieved by synthesizing

* Corresponding author. Address: Engineering Science, EA 07-37, Department of Electrical and Computer Engineering, 4 Engineering Drive 3, National University of Singapore, Singapore 117576. Tel: (65) 6516 8121. Fax: (65) 67754710. E-mail: elehw@nus.edu.sg.

Received for review February 09, 2010 and accepted June 24, 2010

[†] Department of Electrical and Computer Engineering, National University of Singapore.

[‡] Agency for Science Technology and Research.

[§] Nanoscience and Nanotechnology Initiative, Faculty of Engineering, National University of Singapore.

DOI: 10.1021/am100421e

2010 American Chemical Society

smaller nanoparticles. On the contrary, good light scattering can be achieved either by employing larger nanoparticles or addition of scattering layers (32–34). The usual consequence is that films with high surface area (small nanoparticles) exhibit poor light scattering, whereas films with good light scattering (big nanoparticles) end up with smaller surface area for dye adsorption.

The objective of this work is to synthesize mesoporous TiO₂ film with high surface area and good light scattering properties. This is achieved by incorporating P25 nanoparticles of ~30 nm diameter into the mesoporous TiO₂ matrix. The P25 nanoparticles serve as active binder to form thick films (~10 μm) without cracks and to enhance the scattering of the incoming light.

2. EXPERIMENTAL DETAILS

The mesoporous TiO₂ was synthesized via the evaporation-induced self-assembly route. The amount of Pluronic P123 was varied between 1.0 and 2.0 g in 20 g of ethanol to investigate its effect on the pore structure. Subsequently, 3.4 g of titanium ethoxide and 0.3 mL of concentrated HCl were added into the solution. Dip coating, based on the solvent evaporation technique, was used to prepare the mesoporous films. The detailed procedure is described elsewhere (35). The synthesized solution was dried at room temperature to form a gel. The gel was converted into fine paste using DI water, and then spread on fluorine-doped tin oxide (FTO) glass (resistivity 15 ohm per square) by doctor blade technique. No binder was used in this preparation. The films were allowed to dry in ambient conditions before heating at various temperatures of 350–550 °C for 30 min in air. However, the mesoporous TiO₂ film was found to crack after the heat treatment. Hence, Degussa P25 nanoparticles (Aerosil, ~30 nm, BET 56 m²/g) were added into the mesoporous TiO₂ gel at 5% concentration by weight to obtain mesoporous/P25 mixture films.

To make the dye-sensitized solar cell (DSSC), we immersed the films in an ethanolic solution containing 0.3 mM Ru-dye, (*cis*-dithiocyanate-*N,N'*-bis(4-carboxylate-4 tetrabutyl ammoniumcarboxylate-2,2'-bipyridine) ruthenium(II) (known as N719, Solaronix), for 24 h at room temperature. Subsequently, the films were rinsed with ethanol. Platinum-coated FTO was used as the counter electrode. The redox electrolyte was prepared with 0.1 M LiI, 0.05 M I₂, 0.6 M 1,2-dimethyl-3-propylimidazolium iodide, and 0.5 M 4-*tert*-butylpyridine in acetonitrile. Three cells with different working electrodes, namely P25 nanoparticles, mesoporous TiO₂, and mesoporous/P25 (P25 nanoparticles and TiO₂ mesoporous), were made.

The morphology of synthesized TiO₂ films was obtained using JEOL-2100 high-resolution transmission electron microscope (HRTEM) with accelerating voltage of 200 kV, along with selected area electron diffraction (SAED) pattern and JEOL FEG JSM 6700 F field-emission scanning electron microscope (FESEM) operating at 10 kV. The film thickness was measured using Ambios Technology XP 200 profilometer. Structural characterization of the synthesized films was done using X-ray diffraction (XRD) on Philips X-ray diffractometer with CuKα radiation ($\lambda = 1.541 \text{ \AA}$). Brunauer–Emmett–Teller (BET) measurements were conducted using Quantachrome Nova 1200 with N₂ as the adsorbate at liquid nitrogen temperature. The amount of dye absorbed on the different TiO₂ films was estimated using UV–vis spectrophotometer (UV-1800 Shimadzu). The photocurrent–voltage of the samples was measured with a AM1.5 solar simulator (Newport Inst., model 91160A) with an AM filter (81088A). A 150 W Xe lamp was used as the light source. The photoelectrochemical performance of the solar cells was measured at 25

°C with a sourcemeter (Keithley 2420) and Newport IV test station software. The light intensity corresponding to AM 1.5 (100 mW/cm²) was calibrated using a standard silicon solar cell (Oriel, SRC-1000-TC). The lamp provides uniform illumination in the area of 10 × 10 cm². Incident photon-to-collected-electron conversion efficiency (IPCE) spectra were measured with a spectral resolution of 5 nm using a 300 W xenon lamp and a grating monochromator equipped with order sorting filters (Newport/Oriel). The incident photon flux was determined using a calibrated silicon photodiode (Newport/Oriel). Photocurrents were measured using an autoranging current amplifier (Newport/Oriel). The control of the monochromator and recording of photocurrent spectra were performed using the TRACQ Basic software (Newport). Electrochemical impedance spectroscopy (EIS) was recorded using a potentiostat PGSTAT 302N (Autolab, Eco Chemie) under illumination of 100 mW cm⁻². The frequency range was varied from 5 mHz to 100 kHz and magnitude of the alternating signal was 10 mV.

3. RESULTS AND DISCUSSION

Tuning of pore morphologies is carried out to study the effects on dye loading capability. In addition, optimum thickness of the film with good adherence to FTO is covered. Pores can be tuned via the self-organization of TiO₂ nanoparticles, which is directly related to the block copolymer P123 template. P123 amphiphilic triblock copolymer is a nonionic surfactant with hydrophilicity between the polyethylene oxide (PEO) and polypropylene oxide (PPO) chains as the driving force to form micelles. The synthesis of the mesoporous structure is based on the evaporation of an organic solvent promoting self-assembly of the surfactant and the simultaneous condensation of the inorganic oxide precursor. The aging temperature is controlled at 13 °C to promote full condensation and self-assembly of nanostructures. Figure 1 shows mesoporous TiO₂ films synthesized with different amount of block copolymer. In general, when 1.0 and 1.5 g of P123 is used, well-structured pores are obtained as shown in images a and b in Figure 1, respectively. High magnification shows that the film has a high density of quasi-hexagonal pores of ~10 nm in diameter. When the copolymer concentration is increased to 2.0 g, stripes of lamellar pores are observed (Figure 1c). It is noted that transformation to lamellar pores occurs when copolymer micelles aggregate. The aggregation takes place above a certain critical micelle concentration (CMC). It is noteworthy that the tuning of the pore structure with two different types of alignments is due to the micellar packing, quasi-hexagonal pores resulting from the spherical micelles and stripes of aligned pores resulting from cylindrical micelles (36).

Other than the formation of well-structured pores, the crystallinity and stability of the porous framework are also taken into account. Thus, changes in morphology of the film are studied by varying the calcination temperature. Film calcined at 350 °C shows well-ordered pores, but is amorphous in nature (TEM result not shown here). Figure 1d shows mesoporous TiO₂ film calcined at 450 °C. The film retains the well-structured quasi hexagonal pores. However, at higher temperatures of 500 and 550 °C, the ordered matrixes of the pores collapse (Figure 1e,f). The film structures are also investigated using TEM. Low-resolution TEM

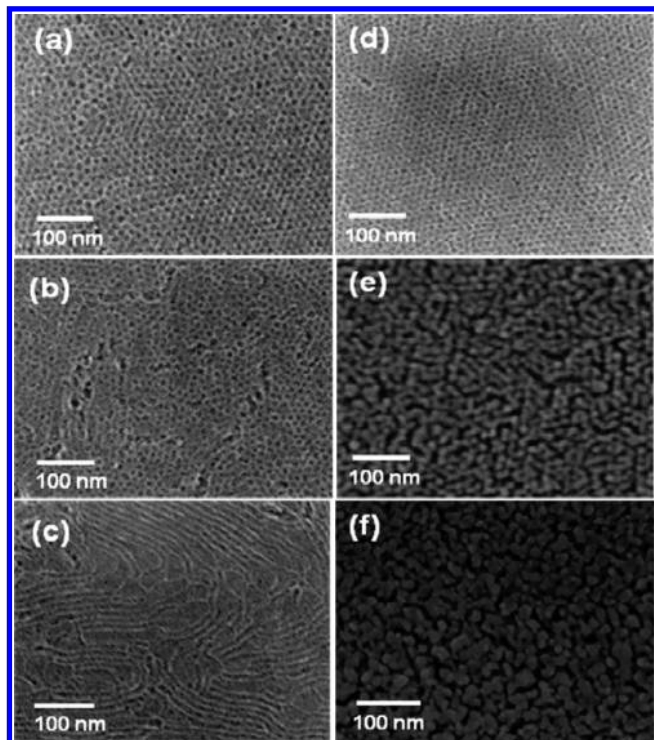


FIGURE 1. SEM images of (a, b) quasi hexagonal and (c) lamellar pores at various copolymer concentrations. Calcined films at (d) 450, (e) 500, and (f) 550 °C.

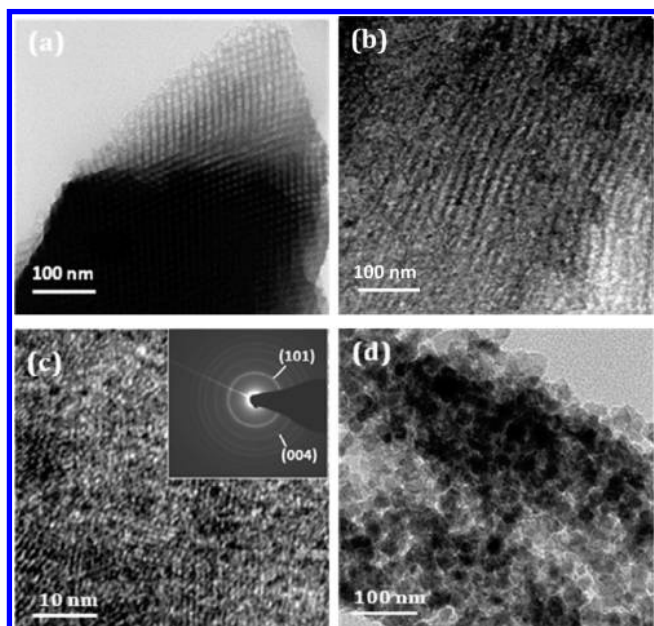


FIGURE 2. (a, b) Low- and (c, d) high-resolution TEM images of (c) 450 °C annealed mesoporous TiO₂ (inset: selected electron diffraction pattern) and (d) 550 °C annealed mesoporous TiO₂.

images (Figure 2a,b) show short-range ordering of the pores. Lattice fringes of (101) plane of TiO₂ are revealed in Figure 2c, with an interplanar spacing d value of ~ 0.36 nm. The electron diffraction pattern (inset in Figure 2c) displays the Debye–Scherrer rings of TiO₂. Diffraction rings are indexed as (101) and (004), which suggest the formation of crystalline anatase TiO₂ film. Hence, as the temperature increases from 350 to 550 °C, crystallinity improves, whereas ordering of the mesoporous structure deteriorates. The collapse of the

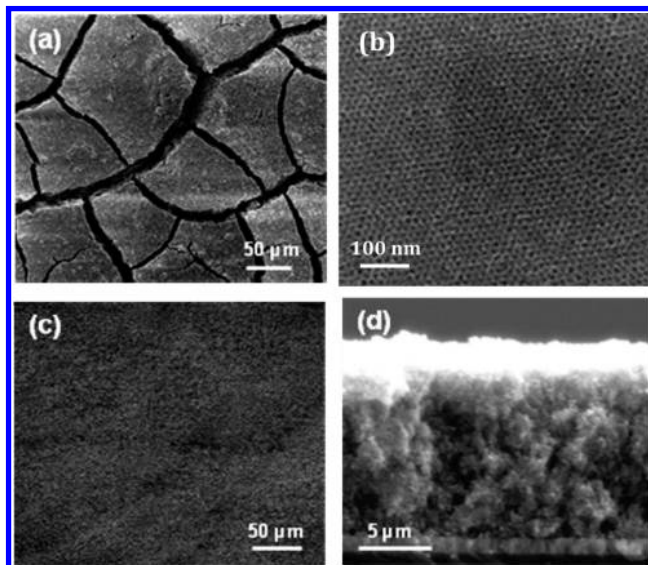


FIGURE 3. (a) Low- and (b) high-magnification SEM images of mesoporous TiO₂ film. SEM images of (c) top and (d) cross-sectional views of mesoporous/P25 film.

quasi-hexagonal pores and the aggregation of TiO₂ nanoparticles are clearly observed for the mesoporous TiO₂ film calcined at 550 °C (Figure 2d). Thus, calcination temperature of 450 °C is optimized to achieve high crystallinity without compromising the stability of the porous framework.

The optimized mesoporous TiO₂ film with good crystallinity and stable pore structure is doctor bladed on the FTO glass. Thick TiO₂ films of ~ 10 μm are prepared. However, a thick mesoporous TiO₂ film (Figure 3a) is observed to crack, leading to a poor film quality. The mesoporous TiO₂ film shows numerous cracks of \sim tens to hundreds of micrometer in length across the whole surface (Figure 3a). Though the film shows numerous microcracks, ordered quasi-hexagonal pores can still be observed at high magnification (Figure 3b). The cracking issue is caused by the stress induced during the film shrinkage because of the decomposition of the triblock copolymer and crystallization of the film (30). The film cracking is prominent with thicker films. Subsequently, P25 nanoparticles of ~ 30 nm diameter are added to the mesoporous TiO₂, essentially functioning as active binder. The nanoparticles are shown to be effective in binding the mesoporous matrix, thus circumventing delamination and cracking issues. Images c and d in Figure 3 show the SEM top and cross-sectional views of the mesoporous/P25 (TiO₂ mesoporous and P25 nanoparticle) film. The mesoporous/P25 film is uniform and crack-free and shows no delamination from the FTO substrate.

Three types of thick films, namely the P25 nanoparticles, mesoporous TiO₂, and mesoporous/P25 are prepared and calcined at 450 °C. Figure 4a shows the XRD patterns of all the calcined samples. The mesoporous TiO₂ film shows well-resolved and sharp peaks of anatase phase. The crystallinity and planes of this mesoporous TiO₂ film are consistent with the SAED results as discussed earlier. It is noted that the high degree of crystallinity is necessary for efficient photovoltaic operation. TiO₂ rutile phase has been reported to exhibit lower efficiency than the anatase phase (37). This is due to

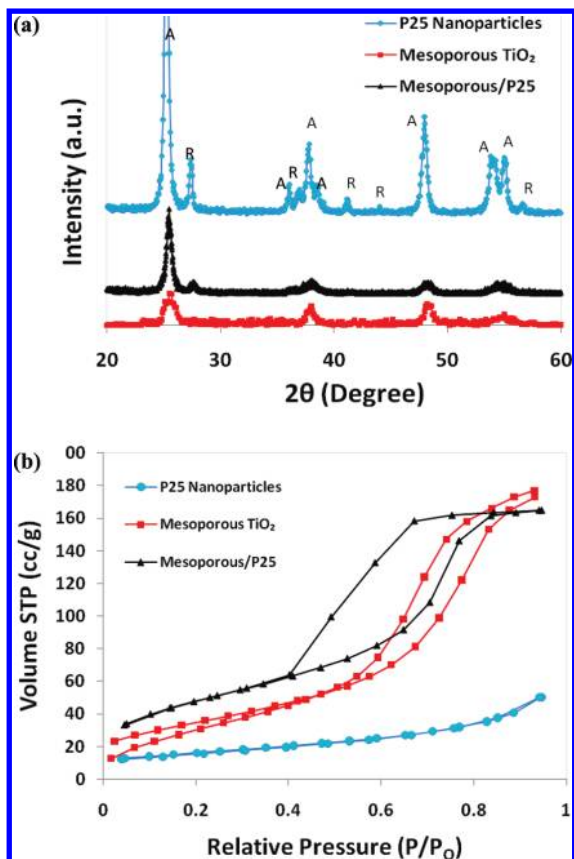


FIGURE 4. (a) XRD and (b) nitrogen adsorption–desorption spectra of P25 nanoparticles, mesoporous TiO₂ and mesoporous/P25 films. A represents the anatase and R the rutile phase of TiO₂.

the close packing nature of rutile phase, which leads to the lower surface area (38). Moreover, electron transport is relatively faster in the anatase phase than the rutile phase, as anatase phase has higher conduction-band edge energy (39). Hence, anatase is the preferred phase for efficient functioning of the DSSC. Thus, it is important to analyze the amount of anatase and rutile phases present in each sample by taking the ratio of the two most intense peaks of the anatase I_A (101) and rutile I_R (110) (40). P25 nanoparticle spectra shows composition of both anatase (~80%) and rutile phase (~20%), whereas mesoporous TiO₂ spectra exhibits pure anatase phase. Adding P25 nanoparticles (5 wt %) into the mesoporous TiO₂ introduces a small amount of rutile phase (~12%) in the mesoporous/P25 film, although anatase remains the dominant phase (~88%). The approximate crystallite sizes of the samples are calculated using Scherrer's formula (41) and are summarized in Table 1. The calculated crystallite sizes of the P25 nanoparticles, TiO₂ mesoporous, and mesoporous/P25 films are 29, 10, and 15 nm, respectively.

Table 1 summarizes the various parameters obtained from BET characterization for the three samples. The specific surface area of the mesoporous TiO₂ is found to be 189 m²/g, which is about 3.4 times higher than the surface area of P25 nanoparticles (56 m²/g). The addition of TiO₂ nanoparticles to mesoporous matrix does not change the surface area (180 m²/g) significantly. High-surface-area film is de-

sired for increased dye absorption (15). The particle size D is given by the following equation

$$D = 6000/[S_{\text{BET}}\rho] \quad (1)$$

where S_{BET} is the BET specific surface area and ρ is the density of the TiO₂ (4.2 g/mL). The average particle size is estimated by assuming that the particles are spherical in shape and have similar density. These assumptions will introduce some inaccuracies in the calculated values, especially for the mesoporous/P25 sample. The particle size obtained by BET method shows a similar trend as the crystallite size calculated from the Scherrer's formula, though large discrepancies in the calculated values are expected.

Figure 4b reveals N₂ adsorption–desorption isotherms for all the samples. The mesoporous TiO₂ and mesoporous/P25 samples exhibit type IV nitrogen isotherm while the P25 nanoparticles exhibit a type III isotherm. Type III isotherm has adsorption and desorption branches that coincide, as no adsorption–desorption hysteresis is displayed, indicating a nonporous material. The adsorption of mesoporous TiO₂ and mesoporous/P25 samples proceeds via multilayer adsorption followed by capillary condensation. This adsorption process is initially similar to that of the macroporous solids, but at higher pressures, the amount adsorbed rises very steeply because of the capillary condensation in the mesopores. The capillary condensation and evaporation do not take place at the same pressure, thus leading to the formation of hysteresis loops. The isotherm of the mesoporous TiO₂ exhibits hysteresis loop of type H1, as it displays parallel and nearly vertical branches between the adsorption and desorption isotherms. The H1 hysteresis typically represents the materials with cylindrical pore geometry and high degree of pore size uniformity (42). The isotherm of mesoporous/P25 seems to be an intermediate between Type H1 and H3. H3 hysteresis loop does not level off at relative pressures close to the saturation vapor pressure. It signifies that material comprises of aggregates of mesoporous particles (42). This implies that mesoporosity of the mesoporous TiO₂ is not lost after mixing the P25 nanoparticles into it. It can be seen from Figure 4b that the monolayer adsorption for the mesoporous TiO₂ is completed at a relative pressure of 0.4. However, the monolayer adsorption for mesoporous/P25 is not completed until it reaches a relative pressure of 0.6. This indicates that mesoporous TiO₂ possesses much smaller pore size than the mesoporous/P25 sample. The pores in mesoporous TiO₂ originate from triblock copolymer micelles which have been removed after calcination. On the other hand, the mesoporous/P25 film has larger pores ~16 nm (Table 1). These pores are presumably formed by the aggregation of small mesoporous TiO₂ particles with larger P25 nanoparticles when calcination is performed. Larger pores are expected to have better electrolyte/dye wetting and filling, which prevent charge from building up, thus reducing the amount of recombination.

The adsorption of the N719 dye molecules in the three films are compared before cell construction (Figure 5a). The

Table 1. Physical Properties of P25 Nanoparticles, Mesoporous TiO₂, and Mesoporous/P25 Films

sample	anatase %	rutile %	crystallite size ^a (nm)	particle size ^b (nm)	surface area (m ² /g)	pore size (nm)	dye adsorbed (mol/cm ³)
P25	80	20	29	25.5	56	12	6.1×10^{-7}
mesoporous TiO ₂	100	0	10	7.5	189	9	4.7×10^{-7}
mesoporous/P25	88	12	15	8.0	180	16	1.5×10^{-6}

^a XRD method. ^b BET method

amount of dye loaded in each sample is obtained by desorbing the samples into 0.02 M NaOH in 4 mL of ethanol. All the samples are 4 cm² in size with a thickness of approximately 10 μm. All ruthenium-based dyes exhibit ligand-centered charge transfer (LCCT) transitions ($\pi-\pi^*$), as well as metal-to-ligand charge transfer (MLCT) transitions ($4d-\pi^*$). N719 dye shows the absorption maxima at 380 and 518 nm. The distinct peaks seen at ~372 and 509 nm for the P25 nanoparticles, mesoporous TiO₂, and mesoporous/P25 films are attributed to the MLCT transfer absorption band of N719 dye. A small shift (~10 nm) is observed in the MLCT peaks of the dye loaded samples as compared to the peaks of N719 dye. This is due to the interactions of the dye molecules with the TiO₂ films. The dye loading capabilities of all the films are shown in Table 1. The results show relatively higher dye absorbance of the mesoporous/P25 film compared to the other two homogeneous (P25 nanoparticles and mesoporous TiO₂) samples. This may be attributed to

the presence of relatively larger pores, which is expected to have better dye wetting and loading. The mesoporous film has lower dye loading capability because of film cracking and delamination.

Light-scattering properties of the various TiO₂ films are investigated (Figure 5b). If the incident light is reflected back into the cell, it enhances the absorption of the dye in the cell. It can be observed that the mesoporous/P25 film exhibits an improved reflectance over the mesoporous TiO₂ film, although the P25 nanoparticles film shows the highest reflectance properties. This suggests that the addition of larger nanoparticles promotes the light scattering, which contributes to an increased diffuse reflectance. It can also be seen that the mesoporous/P25 films possess good reflectance characteristics both in the short and long wavelength region (350–800 nm), unlike the mesoporous TiO₂ film,

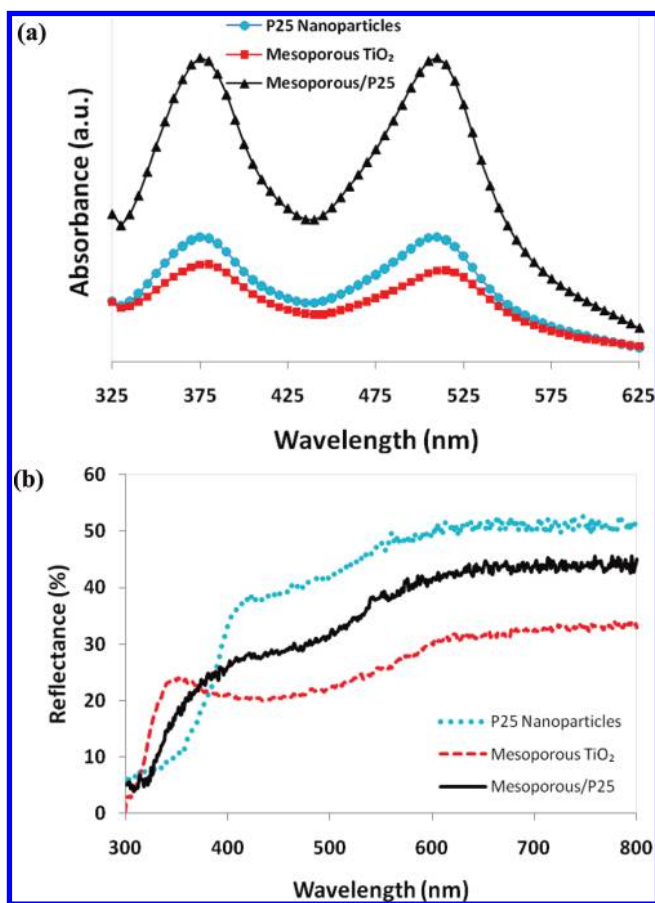


FIGURE 5. (a) UV-vis absorption of dye loaded samples and (b) diffused reflectance spectra of P25 nanoparticles, mesoporous TiO₂, and mesoporous/P25 films.

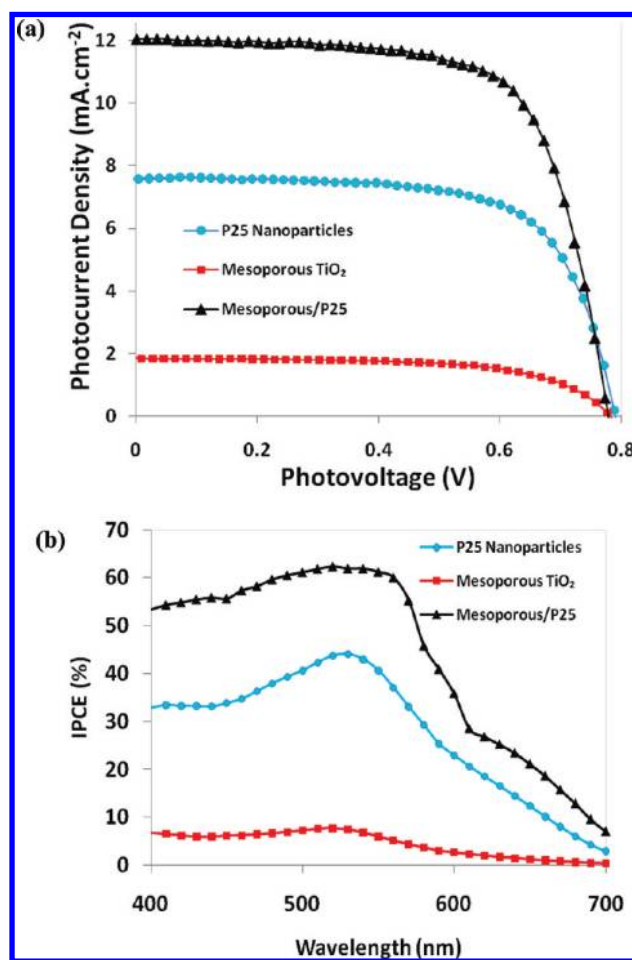


FIGURE 6. (a) Current density-voltage and (b) IPCE curves of DSSC made from P25 nanoparticles, mesoporous TiO₂, and mesoporous/P25 films.

Table 2. Photovoltaic and Series Resistance Data of Three Different TiO₂ Films

DSSC	V_{oc} (V)	J_{sc} (mA/cm ²)	FF (%)	η (%)	R_{Voc}^a (Ω)	$R_{J_{sc}}^a$ (Ω)	R_s^b	R_{ct}^b	W_s-R
P25	0.7	7.6	67.9	4.0	41.5	16436.5	12.4	11.7	142.7
mesoporous TiO ₂	0.7	1.8	63.0	0.9	70.9	15172.3	41.8	12.3	148.6
mesoporous/P25	0.7	12.2	69.5	6.5	32.1	10378.9	14.0	9.1	25.3

^a From $I-V$ measurements. ^b From EIS.

which has a slight dip in reflectance at 400–600 nm. From the reflectance spectra, it is apparent that there is an improvement of ~25–35% in the reflectance (visible light range) because of the contribution of larger P25 nanoparticles in the mesoporous/P25 films.

Figure 6a displays the photocurrent density voltage characteristics of the cells made from different films under simulated irradiation (global AM 1.5, 100 mW/cm²). Table 2 shows the summary of photovoltaic and series resistance data of different films. The active area of the electrodes is 0.25 cm². The low efficiency of the mesoporous TiO₂ film (<1%) is due to the presence of microcracks that lead to poor adhesion of the film to the photoanode. As can be seen, the current density of the mesoporous/P25 film is about 1.6 and 7.2 times higher than homogeneous P25 nanoparticles and mesoporous TiO₂ DSSC, respectively. These results suggest better charge injection and transportation of photoexcited electrons in the mesoporous/P25 DSSC. The increase in the fill factor (FF) of the mesoporous/P25 film DSSC indicates the suppression of the charge recombination process at the TiO₂/dye/electrolyte interface. Hence, the DSSC mesoporous/P25 film gives a higher efficiency of 6.5% than the other two DSSC (P25 nanoparticles and mesoporous TiO₂). To ascertain the reproducibility of the results for the DSSC using mixture of mesoporous TiO₂ and P25, various statistics on the efficiency and other parameters for the DSSC has been plotted (see the Supporting Information, Figure S1). The series resistance comprises of the resistance for electron transport in the FTO substrate (R_s), resistance for the electron transfer across the interface of electrolyte/Pt-FTO (R_{ct}), and the Nernst diffusion impedance (W_s) within the electrolyte (W_s-R). The various resistance values were calculated from EIS, which is a powerful technique to identify and study the transport and recombination in DSSC. The various resistances obtained from EIS show similar trend as those obtained from solar simulator IV measurements. The series resistance is lowest for the mesoporous/P25 device. The pure mesoporous TiO₂ film shows high series resistance due to high recombination resulting from cracked film. It is well-known that the IPCE is influenced by the light-harvesting efficiency, electron-transfer yield, and electron-collecting efficiency in the external circuit. Figure 6b shows the IPCE spectra obtained for the three DSSC. The absolute IPCE for the mesoporous/P25 DSSC is significantly higher than the other two DSSC over the entire wavelength region. This result is in good agreement with the high short-circuit photocurrent density observed in the solar cell. The increase in efficiency may be attributed to many factors. First, the mesoporous/P25 film is crystalline and predominantly anatase phase, which helps in better electron transport. Second, the high surface area of the mesoporous/P25 film helps in

better dye adsorption. Third, adding larger P25 nanoparticles of ~30 nm helps in better light scattering. Lastly, mesoporous structure of mesoporous/P25 film helps in rapid and efficient interfacial electron transfer between TiO₂, dye, and redox active species of the electrolyte.

4. CONCLUSION

We have demonstrated systematic tuning of pores that resulted in two different types of micellar packing. The calcination temperature is optimized at 450 °C to obtain a well-crystalline and stable porous framework. The synthesized mesoporous TiO₂ film shows poor adhesion to FTO substrate, leading to microcracks formation. Hence, P25 nanoparticles are incorporated into the mesoporous framework, acting as a binder to prevent delamination. The resultant film has predominantly anatase phase, high surface area, bigger pore diameter, and high diffuse reflectance. The photocurrent density of the DSSC made from mesoporous/P25 film is 1.6 and 7.2 times higher than the other two homogeneous TiO₂ films. An overall current conversion efficiency of 6.5% has been achieved for this film. The enhanced photovoltaic performance is a result of uniform crack-free film, better dye loading, and improved light-harvesting capability of the modified film.

Acknowledgment. This work is supported by the National University of Singapore Grant R 533 000 003 112/133 and Applied Materials.

Supporting Information Available: Various statistics on the efficiency and other parameters for DSSC (PDF). This material is available free of charge via the Internet at <http://pubs.acs.org>.

REFERENCES AND NOTES

- O'Regan, B.; Grätzel, M. *Nature* **1991**, *353*, 737–740.
- Nazeruddin, M. K.; Kay, A.; Podicio, I.; Humphry-Baker, R.; Müller, E.; Liska, P.; Vlachopoulos, N.; Grätzel, M. *J. Am. Chem. Soc.* **1993**, *115*, 6382–6390.
- Kang, M. -S.; Kim, Y. J.; Won, J.; Kang, Y. S. *Chem. Commun.* **2005**, *21*, 2686–2688.
- Kang, M. -S.; Kim, J. H.; Kim, Y. J.; Won, J.; Park, N. G.; Kang, Y. S. *Chem. Commun.* **2005**, *7*, 889–891.
- Law, M.; Greene, L. E.; Johnson, J. C.; Saykally, R.; Yang, P. *Nat. Mater.* **2005**, *4*, 455–459.
- Jose, R.; Kumar, A.; Thavasi, V.; Ramakrishna, R. *Nanotechnology* **2008**, *19*, 424004.
- Stergiopoulos, T.; Valota, A.; Likodimos, V.; Spiliotis, Th.; Niarchos, D.; Skeldon, P.; Thompson, G. E.; Falaras, P. *Nanotechnology* **2009**, *20*, 365601.
- Oh, J. K.; Lee, J. K.; Kim, H. S.; Han, S. B.; Park, K. W. *Chem. Mater.* **2010**, *22*, 1114–1118.
- Maciak, E.; Opilski, Z. *Thin Solid Films* **2007**, *515*, 8351–8355.
- Manera, M. G.; Spadavecchia, J.; Buso, D.; Fernández, C.; de, J.; Mattei, G.; Martucci, A.; Mulvaney, P.; Pérez-Juste, J.; Rella, R.; Vasanelli, L.; Mazzoldi, P. *Sens. Actuators, B* **2008**, *132*, 107–115.
- Campus, F.; Bonhote, P.; Grätzel, M.; Heinen, S.; Walder, L. *Sol. Energy Mater. Sol. Cells* **1999**, *56*, 281–297.

- (12) Partlow, D. P.; O'Keeffe, T. W. *Appl. Opt.* **1990**, *29*, 1526–1529.
- (13) Brudnik, A.; Cztenastek, H.; Zakrzewska, K.; Jachimowski, M. *Thin Solid Films* **1991**, *199*, 45–58.
- (14) Yang, L.; Saavedra, S. S.; Armstrong, N. R. *J. Anal. Chem.* **1994**, *66*, 1254–1263, Hayes.
- (15) Li, X.; Green, A. N. M.; Haque, S. A.; Mills, A.; Durrant, J. R. *J. Photochem. Photobiol., A: Chem.* **2004**, *162*, 253–259.
- (16) Zhao, D.; Huo, Q.; Feng, J.; Chmelka, B. F.; Stuckey, G. D. *J. Am. Chem. Soc.* **1998**, *120*, 6024–6036.
- (17) Coakley, K. M.; Liu, Y.; McGehee, M. D.; Frindell, K. L.; Stucky, G. D. *Adv. Funct. Mater.* **2003**, *13*, 301–306.
- (18) Jain, A.; Toombes, G. E. S.; Hall, L. M.; Mahajan, S.; Garcia, C. B. W.; Probst, W.; Gruner, S. M.; Wiesner, U. *Angew. Chem., Int. Ed.* **2005**, *44*, 1226–1229.
- (19) Warren, S. C.; Messina, L. C.; Slaughter, L. S.; Kamperman, M.; Zhou, Q.; Gruner, S. M.; DiSalvo, F. J.; Wiesner, U. *Science* **2008**, *320*, 1748–1752.
- (20) Coakley, K. M.; McGehee, M. D. *Appl. Phys. Lett.* **2003**, *83*, 3380.
- (21) Kaune, G.; Memesa, M.; Meier, R.; Ruderer, M. A.; Diethert, A.; Roth, S. V.; D'Acunzi, M.; Gutmann, J. S.; Buschbaum, P. M. *Appl. Mater. Interface* **2009**, *1*, 2862–2869.
- (22) Zukalova, M.; Zukal, A.; Kavan, L.; Nazeeruddin, M. K.; Liska, P.; Grätzel, M. *Nano Lett.* **2005**, *5*, 1789–1792.
- (23) Chena, Y.; Stathatos, E.; Dionysiou, D. D. *J. Photochem. Photobiol., A* **2009**, *203*, 192–198.
- (24) Nedelcu, M.; Lee, J.; Crossland, E. J. W.; Warren, S. C.; Orilall, M. C.; Guldin, S.; Hüttner, S.; Ducati, C.; Eder, D.; Wiesner, U.; Steiner, U.; Snaith, H. J. *Soft Matter* **2009**, *5*, 134–139.
- (25) Wei, M.; Konishi, Y.; Zhou, H.; Yanagida, M.; Sugihara, H.; Arakawa, H. *J. Mater. Chem.* **2006**, *16*, 1287–1293.
- (26) Kambe, S.; Murakoshi, K.; Kitamura, T.; Wada, Y.; Yanagida, S.; Kominami, H.; Kera, Y. *Sol. Energy Mater. Sol. Cells* **2000**, *6*, 427–441.
- (27) Zukalová, M.; Procházka, J.; Zukal, A.; Yum, J. H.; Kavan, L. *Inorg. Chim. Acta* **2008**, *361*, 656–662.
- (28) Hou, K.; Tian, B.; Li, F.; Bian, Z.; Zhao, D.; Huang, C. *J. Mater. Chem.* **2005**, *15*, 2414–2420.
- (29) Wei, M.; Wang, K.; Yanagida, M.; Sugihara, H.; Morris, M. A.; Holmes, J. D.; Zhou, H. *J. Mater. Chem.* **2007**, *17*, 3888–3893.
- (30) Kajihara, K.; Yao, T. *J. Sol-Gel Sci. Technol.* **2000**, *17*, 173–184.
- (31) Lee, J.; Orilall, M. C.; Warren, S. C.; Kamperman, M.; DiSalvo, F. J.; Wiesner, U. *Nat. Mater.* **2008**, *7*, 222–228.
- (32) Kroon, J. M.; Baker, N. J.; Smit, H. J. P.; Liska, P.; Thampi, K. R.; Grätzel, M.; Hinsch, A.; Hore, S.; Durrant, J. R.; Palomares, E.; Pettersson, H.; Gruszecki, T.; Walter, J.; Skupien, K.; Tulloch, G. In *Proceedings of the 19th European Photovoltaic Solar Energy Conference*; Paris, June 7–11, 2004; Joint Research Centre, European Commission: Brussels, Belgium, 2004.
- (33) Koo, H. J.; Park, J.; Yoo, B.; Yoo, K.; Kim, K.; Park, N. G. *Inorg. Chim. Acta* **2008**, *361*, 677–683.
- (34) Kanga, S. H.; Kima, J. Y.; Kima, H. S.; Kohb, H. D.; Leeb, J. S.; Sung, Y. E. *J. Photochem. Photobiol., A* **2008**, *200*, 294–300.
- (35) Agarwala, S.; Ho, G. W. *Mater. Lett.* **2009**, *6*, 1624–1627.
- (36) Yong, M. J. Q.; Wong, A. S. W.; Ho, G. W. *Mater. Chem. Phys.* **2009**, *116*, 563–568.
- (37) Park, N. G.; Van de Lagemaat, J.; Frank, A. J. *J. Phys. Chem. B* **2000**, *104*, 8989–8994.
- (38) Kalyanasundaram, K.; Grätzel, M. *Coord. Chem. Rev.* **1998**, *177*, 347–414.
- (39) Wold, A. *Chem. Mater.* **1993**, *5*, 280–283.
- (40) Spurr, R. A.; Myers, W. *Anal. Chem.* **1957**, *29*, 760–762.
- (41) Cullity, B. D. *Elements of X-ray Diffraction*, 2nd ed.; Addison-Wesley: Reading, MA, 1978.
- (42) Kruk, M.; Jaroniec, M. *Chem. Mater.* **2001**, *13*, 3169–3185.

AM100421E